Numerical modelling of basin irrigation with an upwind scheme

P. Brufau, P. García-Navarro [1], E. Playán, N. Zapata [2]

June 30, 2000

---

[1] Fluid Mechanics. Centro Politécnico Superior. University of Zaragoza.
[2] Laboratory of Agronomy and the Environment (DGA-CSIC), EEAD, CSIC

Abstract

In recent years, upwind techniques have been successfully applied in hydrology to simulate two-dimensional free surface flows. Basin irrigation is a surface irrigation system characterized by its potential to use water very efficiently. In basin irrigation, the field is leveled to zero slope and flooded from a point source. The quality of land leveling has been shown to influence irrigation performance drastically. Recently, two-dimensional numerical models have been developed as tools to design and manage basin irrigation systems. In this work, a finite volume based upwind scheme is used to build a simulation model considering differences in bottom level. The discretization is made on triangular unstructured grids and the source terms of the equations are given a special treatment. The model is applied to the simulation of two field experiments.

1 Introduction

Many efforts have been recently devoted to the development of multidimensional techniques for free surface flows. Among them, those oriented to the resolution of unsteady shallow water flow, have been strongly influenced by the upwind philosophy initially introduced in Gas Dynamics. These methods are specially suited for advection dominated problems and their implementation is not straightforward when source terms are relevant.[3,4]

Numerical models of overland flow have been applied to a number of practical problems of interest in Engineering, including overland hydrology, open channel management and surface irrigation. In the domain of surface irrigation, this type of numerical models are particularly interesting for the simulation of basin irrigation. Basin irrigation (also known as level-basin irrigation) consists on flooding a squarish, relatively large field, leveled to zero average slope and fully surrounded by a dike to prevent runoff.[19] The idea behind basin irrigation is very simple, although its real world applications have been limited by the difficulty to level the basin with the accuracy required to flood the field quickly and uniformly. The main design and management variables in basin irrigation are the irrigation discharge, the irrigation time, the field geometry and the quality of land leveling (often represented by the standard deviation of bottom level).

The first attempts to simulate basin irrigation used one-dimensional models.[6] The limitations of this approach stem form the marked two-dimensional character of the flow, particularly in the presence of point inflows and irregular geometries. Two-dimensional models were applied to the simulation of basin irrigation,[11,17] using explicit finite difference methods. A leapfrog finite difference method was used to explore the relationship between the quality of land leveling and irrigation performance.[12,20] The comparison of simulation results with experimental data revealed limitations in the numerical models. In fact, the experiment reported by Zapata and Playán[20] represents a difficult simulation case, in which the advance of water in a small experimental basin is strongly dictated by differences in elevation. These authors performed simulations using alternatively a flat bed and a bed with the observed bottom level. The advance curve (flooded area vs. time) was best reproduced when bottom level was supplied to the model. However, even in this case, the model overestimated the advance rate. The predicted location of the advancing front revealed the main trends observed in the field, but lacked much of the experimental detail.

In this work, an upwind scheme is used to build a basin irrigation simulation model considering differences in bottom level. Model features are discussed in the text and the model is applied to reproduce two field experiments illustrating the relevance of land leveling on basin irrigation performance.

2 Governing equations

The flow of overland water during surface irrigation is in general governed by the continuity and momentum laws of fluid mechanics applied to a free surface incompressible flow over a pervious bed. Given the different size of the vertical and horizontal spatial scales involved in this kind of flow, the shallow water approximation is usually adopted for the mathematical description. By doing so the problem is transformed, the free surface position is no longer a boundary condition nor it is the bed permeability. Instead, the water depth appears as one of the dependent variables and the infiltrated water is taken into account as a source term of the depth averaged mass and momentum equations. This mathematical model for the surface irrigation problem, involving many simplifications of the real features, is among the most complete hydrodynamic models in the literature, and other more simplified forms are frequent.[?]

The equations will be solved by means of a finite volume technique based on an upwind scheme initially designed for systems of conservation laws. Therefore, we are interested in writing the 2D shallow overland flow equations in conservative form,[1]

$$\frac{\partial \mathbf{U}}{\partial t} + \nabla \cdot (\mathbf{F}, \mathbf{G}) = \mathbf{H} \tag{2.1}$$

with

$$\begin{aligned} \mathbf{U} = \begin{pmatrix} h \\ hu \\ hv \end{pmatrix}, \ \mathbf{F} &= \begin{pmatrix} hu \\ hu^2 + g\frac{h^2}{2} \\ huv \end{pmatrix}, \ \mathbf{G} = \begin{pmatrix} hv \\ huv \\ hv^2 + g\frac{h^2}{2} \end{pmatrix}, \\ \mathbf{H} &= \begin{pmatrix} -i \\ gh\left(S_{0x} - S_{fx}\right) + D_{lx} \\ gh\left(S_{0y} - S_{fy}\right) + D_{ly} \end{pmatrix} \end{aligned} \tag{2.2}$$

where $\mathbf{U}$ represents the vector of conserved variables. h is depth of water, hu and hv are the unit discharges along the coordinate directions x, y respectively with u and v the depth averaged velocities and g is the acceleration due to the gravity. $\mathbf{F}$ and $\mathbf{G}$ are the fluxes of the conserved variables across the edges of a control volume. They consist of the convective fluxes together with the hydrostatic pressure gradients.

$\mathbf{H}$ is the source term containing the effects of infiltration, weight of fluid and bed roughness on the mass and momentum conservation. S_{0x}, S_{0y} are the bed slopes expressed in terms of the bottom depth b in the form

$$S_{0x} = -\frac{\partial b}{\partial x}, \qquad S_{0y} = -\frac{\partial b}{\partial y} \tag{2.3}$$

S_{fx}, S_{fy} are the friction terms in the x, y directions. For the friction term, the Manning equation[5] has been used expressing the energy grade line in terms of the Manning roughness coefficient n as

$$S_{fx} = \frac{n^2 u\sqrt{u^2+v^2}}{h^{\frac{4}{3}}}, \qquad S_{fy} = \frac{n^2 v\sqrt{u^2+v^2}}{h^{\frac{4}{3}}} \tag{2.4}$$

The volume of water lost by infiltration is modelled with the infiltration rate i which can be computed using the empirical Kostiakov-Lewis equation,

$$i = ka\tau^{a-1} + f_0 \tag{2.5}$$

where τ is the time that every point of the field remains wet (opportunity time) expressed in minutes, k and f_0 are coefficients determined by experimental measures and a is an exponent specified by the experiment too. The time integrated form of equation (2.5) provides the expression for z, the infiltrated depth of water in every point of the field.

D_{lx}, D_{ly} account for the momentum transfer associated with seepage outflow in the x, y directions.[11] According to Akanbi and Katopodes,[2] the following approximations are used

$$D_{lx} = \frac{1}{2}ui, \qquad D_{ly} = \frac{1}{2}vi \tag{2.6}$$

3 Numerical model

A cell centered finite volume method is formulated for equation (2.1) over a triangular or quadrilateral control volume where the dependent variables of the system are represented as piecewise constants. The basic method will be first described for the pure conservation law, that is, without source terms. These will be next incorporated and the required modifications indicated. The homogeneous version of equation (2.1) is first written

$$\frac{\partial \mathbf{U}}{\partial t} + \nabla \cdot (\mathbf{F}, \mathbf{G}) = 0 \tag{3.1}$$

then the integral form for a fixed area S is

$$\frac{\partial}{\partial t} \int_S \mathbf{U} dS + \int_S \nabla \cdot (\mathbf{F}, \mathbf{G})\, dS = 0 \tag{3.2}$$

and, applying the divergence theorem to the second integral, we obtain

$$\frac{\partial}{\partial t} \int_S \mathbf{U} dS + \oint_C (\mathbf{F}, \mathbf{G}) \cdot \mathbf{n} dC = 0 \tag{3.3}$$

where C is the boundary of the area S, and $\mathbf{n}$ is the outward unitary normal vector. Given a computational mesh defined by the cells (volumes) of area S_i, where i is the index associated with the centroid of the cell (see Fig. 1) in which the cellwise constant values of $\mathbf{U}$ are stored, equation (3.3) can be represented in every cell by

$$\frac{d\mathbf{U}_i}{dt} S_i + \oint_{C_i} (\mathbf{F}, \mathbf{G}) \cdot \mathbf{n} dC = 0 \tag{3.4}$$

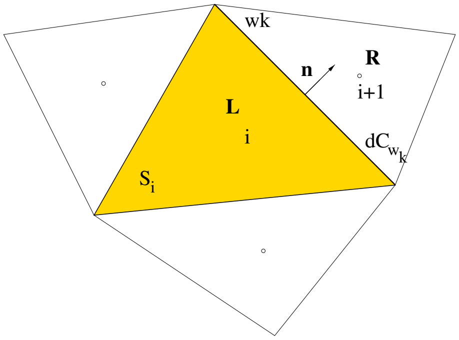

Figure 1: Discretization domain.

The contour integral is next approached via a mid-point rule, i.e., a numerical flux is defined at the mid-point of each edge, giving

$$\oint_{C_i} (\mathbf{F}, \mathbf{G}) \cdot \mathbf{n} dC = \sum_{k=1}^{NE} (\mathbf{F}, \mathbf{G})_k^* \cdot \mathbf{n}_k dC_k \tag{3.5}$$

where k represents the index of the edges of the cell (see Fig. 1), NE is the total number of edges in the cell ($NE = 3$ for triangles, $NE = 4$ for quadrilaterals). The vector $\mathbf{n}_k$ is the unit outward normal, dC_k is the length of the side, and $(\mathbf{F}, \mathbf{G})_k^*$ is the numerical flux tensor.

The evaluation of the numerical flux in equation (3.5) is based on the Riemann problem defined by the conditions on the left and right sides of the cell edges, as in first order MUSCL scheme.[18] An important feature of the 1D Roe's approximate Riemann solver for non-linear systems of equations is exploited here. This is the definition of the approximated flux jacobian, $\tilde{A}_{i+\frac{1}{2}}$,[15] constructed at the edges of the cells. Once this matrix has been defined, the numerical flux across the interface $i + \frac{1}{2}$ between states i on the left (L) and $i + 1$ on the right (R) of a cell in a 1D domain is

$$\mathbf{F}^*_{i+\frac{1}{2}} \quad = \quad \frac{1}{2}\left[\mathbf{F}_{i+1} + \mathbf{F}_i - |\tilde{\mathbf{A}}_{i+\frac{1}{2}}| \left(\mathbf{U}_{i+1} - \mathbf{U}_i\right)\right]$$

$$= \frac{1}{2}\left[\mathbf{F}_R + \mathbf{F}_L - |\tilde{\mathbf{A}}_{RL}| \left(\mathbf{U}_R - \mathbf{U}_L\right)\right] \tag{3.6}$$

The 2D numerical upwind flux in equation (3.5) is obtained by applying the expression (3.6) in a 1D form to each edge k of the computational cell. The 1D philosophy is followed along the normal direction to the cell walls, making use of the normal numerical fluxes, so that

$$(\mathbf{F},\mathbf{G})_k^* \cdot \mathbf{n}_k = \frac{1}{2}\left[(\mathbf{F},\mathbf{G})_R \cdot \mathbf{n}_k + (\mathbf{F},\mathbf{G})_L \cdot \mathbf{n}_k - |\tilde{\mathbf{A}}_{RL}|(\mathbf{U}_R - \mathbf{U}_L)\right] \tag{3.7}$$

Here, R and L denote right and left states respectively at the k edge, $(\tilde{\mathbf{A}}_{RL})$ represents the approximate Jacobian of the normal flux at that edge. Note that subscript k will be omitted for the sake of clarity and the following discussion is referred to cell side k.

The $(\tilde{\mathbf{A}}_{RL})$ matrix must satisfy the following conditions:

- $\tilde{\mathbf{A}}_{RL}$ depends only on the $\mathbf{U}_R$ and $\mathbf{U}_L$ states,
- $(\mathbf{F}_R - \mathbf{F}_L) = \tilde{\mathbf{A}}_{RL}\left(\mathbf{U}_R - \mathbf{U}_L\right)$,
- $\tilde{\mathbf{A}}_{RL}$ has real and distinct eigenvalues and a complete set of eigenvectors,
- $\tilde{\mathbf{A}}_{RL} = \mathbf{A}\left(\mathbf{U}_R\right) = \mathbf{A}\left(\mathbf{U}_L\right)$ if $\mathbf{U}_R = \mathbf{U}_L$

where

$$\mathbf{A} = \frac{\partial\left(\mathbf{F},\mathbf{G}\right)}{\partial \mathbf{U}}\mathbf{n} = \frac{\partial \mathbf{F}}{\partial \mathbf{U}}n_x + \frac{\partial \mathbf{G}}{\partial \mathbf{U}}n_y \tag{3.8}$$

As suggested by Roe[15] the matrix $\tilde{\mathbf{A}}_{RL}$ has the same shape as $\mathbf{A}$ but is evaluated at an average state given by the quantities $\tilde{\mathbf{u}} = (\tilde{u}, \tilde{v})$ and $\tilde{c}$ which must be calculated according to the matrix properties. The approximate Jacobian matrix is not directly used in the actual method. Instead, the difference in the vector $\mathbf{U}$ across a grid edge is decomposed on the matrix eigenvectors basis as

$$\delta \mathbf{U} = \mathbf{U}_R - \mathbf{U}_L = \sum_{m=1}^{3} \alpha_{RL}^m \tilde{\mathbf{e}}_{RL}^m \tag{3.9}$$

where

$$\begin{aligned} \alpha_{RL}^{1,3} &= \frac{\delta h_{RL}}{2} \pm \frac{1}{2\tilde{c}} \left[\delta \left(hu \right)_{RL} n_x + \delta \left(hv \right)_{RL} n_y - \tilde{\mathbf{u}} \cdot \mathbf{n} \delta h_{RL} \right] \\ \alpha_{RL}^2 &= \frac{1}{\tilde{c}} \left[\left(\delta \left(hv \right)_{RL} - \tilde{v} \delta h_{RL} \right) n_x - \left(\delta \left(hu \right)_{RL} - \tilde{u} \delta h_{RL} \right) n_y \right] \end{aligned} \tag{3.10}$$

so that the matrix is replaced by its eigenvalues in the product $|\tilde{\mathbf{A}}_{RL}| (\mathbf{U}_R - \mathbf{U}_L)$. From the eigenvalues of $\mathbf{A}$, those of $\tilde{\mathbf{A}}_{RL}$ have the form

$$\begin{aligned} \tilde{a}^1 &= \tilde{\mathbf{u}} \cdot \mathbf{n} + \tilde{c} \\ \tilde{a}^2 &= \tilde{\mathbf{u}} \cdot \mathbf{n} \\ \tilde{a}^3 &= \tilde{\mathbf{u}} \cdot \mathbf{n} - \tilde{c} \end{aligned} \tag{3.11}$$

where $\tilde{\mathbf{u}} \cdot \mathbf{n} = \tilde{u} n_x + \tilde{v} n_y$, and the eigenvectors are

$$\tilde{\mathbf{e}}^1 = \begin{pmatrix} 1 \\ \tilde{u} + \tilde{c} \cdot n_x \\ \tilde{v} + \tilde{c} \cdot n_y \end{pmatrix} , \ \tilde{\mathbf{e}}^2 = \begin{pmatrix} 0 \\ -\tilde{c} \cdot n_y \\ \tilde{c} \cdot n_x \end{pmatrix} , \ \tilde{\mathbf{e}}^3 = \begin{pmatrix} 1 \\ \tilde{u} - \tilde{c} \cdot n_x \\ \tilde{v} - \tilde{c} \cdot n_y \end{pmatrix} \tag{3.12}$$

They are all in terms of average velocities and celerity. Enforcing the second condition of the matrix $\tilde{\mathbf{A}}_{RL}$ the following expressions for $\tilde{u}$, $\tilde{v}$ and $\tilde{c}$ can be obtained

$$\tilde{u} = \frac{\sqrt{h_R}u_R + \sqrt{h_L}u_L}{\sqrt{h_R} + \sqrt{h_L}}, \quad \tilde{v} = \frac{\sqrt{h_R}v_R + \sqrt{h_L}v_L}{\sqrt{h_R} + \sqrt{h_L}}, \quad \tilde{c} = \sqrt{\frac{g}{2}\left(h_R + h_L\right)} \tag{3.13}$$

It has to be stressed at this point that in case of an advancing front over dry bed the average velocities are calculated in the form

$$\tilde{u} = \frac{u_R + u_L}{2}, \quad \tilde{v} = \frac{v_R + v_L}{2} \tag{3.14}$$

because the velocity values at the right or left cell are zero. However the average value for the celerity is calculated always in the same form, otherwise the balance between the flux and the bed slope is not achieved in steady flow leading to numerical errors (see subsection 3.1).

Once the average quantities have been constructed, expression (3.7) provides the numerical flux normal to each edge of the computational cells.

$$(\mathbf{F},\mathbf{G})_k^* \cdot \mathbf{n}_k = \frac{1}{2}\left[(\mathbf{F},\mathbf{G})_R \cdot \mathbf{n}_k + (\mathbf{F},\mathbf{G})_L \cdot \mathbf{n}_k - \sum_{m=1}^{3} |\tilde{a}_{RL}^m| \alpha_{RL}^m \tilde{\mathbf{e}}_{RL}^m\right] \tag{3.15}$$

We can now substitute it into (3.5), so that (3.4) can be written as

$$\frac{d\mathbf{U}_i}{dt} = -\frac{1}{S_i}\sum_{k=1}^{NE} (\mathbf{F},\mathbf{G})_k^* \cdot \mathbf{n}_k dC_k \tag{3.16}$$

which is an ordinary differential equation and can be integrated by standard methods such as a forward Euler time integration procedure.

$$\mathbf{U}_i^{n+1} = \mathbf{U}_i^n - \frac{\Delta t}{S_i}\left(\sum_{k=1}^{NE} (\mathbf{F},\mathbf{G})_k^* \cdot \mathbf{n}_k dC_k\right)_i^n \tag{3.17}$$

The stability criterion adopted has followed the common used in explicit finite volumes[9] with a little modification. Instead of using the distance between the center of the cell and the center of its neighbour cells d_{ij}, the quantity S_i/P_i is used for stability in case small depths appear and the criterion is the following

$$\delta t \leq min\left[\frac{S_i}{2P_i\left(\sqrt{u^2+v^2}+c\right)_{ij}}\right] \tag{3.18}$$

where S_i is the area of the cell i and P_i the perimeter of the same cell.

The source terms need a special treatment that will be described in the next section. First, it should be noted that the source term vector can be decomposed in three different parts that will be treated separately in next section

$$\mathbf{H} = \mathbf{H}^1 + \mathbf{H}^2 + \mathbf{H}^3 \tag{3.19}$$

corresponding to

$$\mathbf{H}^1 = \begin{pmatrix} 0 \\ ghS_{0x} \\ ghS_{0y} \end{pmatrix} \;,\; \mathbf{H}^2 = \begin{pmatrix} 0 \\ -ghS_{fx} \\ -ghS_{fy} \end{pmatrix} \;,\; \mathbf{H}^3 = \begin{pmatrix} -i \\ D_{lx} \\ D_{ly} \end{pmatrix} \tag{3.20}$$

The first term $\mathbf{H}^1$ accounts for the bed slopes and is the only one containing spatial derivatives. For this reason the discretization procedure will follow the flux term discretization as close as possible as suggested by Bermúdez et al.[4] The second term $\mathbf{H}^2$ accounts for the friction and the third one $\mathbf{H}^3$ contains all the infiltration parameters.

3.1 Source terms: bed slope

An upwind approach has been adopted to model the bottom variations in order to ensure the best balance with the flux terms at least in steady cases. This procedure was studied in detail by Bermúdez and Vázquez-Cendón.[3] The flux discretization can be used in the same way for the bottom slope because both contemplate the same spatial derivative. The development of the upwind discretization for $\mathbf{H}^1$ follows

With the inclusion of this source term, equation (3.1) is converted into

$$\frac{\partial \mathbf{U}}{\partial t} + \nabla \cdot (\mathbf{F}, \mathbf{G}) = \mathbf{H}^1 \tag{3.21}$$

and further transformed into

$$\frac{\partial}{\partial t}\int_S \mathbf{U}\, dS + \oint_C (\mathbf{F}, \mathbf{G}) \cdot \mathbf{n}\, dC = \int_S \mathbf{H}^1 dS \tag{3.22}$$

For the discrete representation, and following the philosophy of the numerical flux function, a numerical source $\mathbf{H}_i^{1*}$ has to be defined as an approach of the surface integral over the cell of the source term $\mathbf{H}^1$.

$$\mathbf{H}_i^{1*} = \int_{S_i} \mathbf{H}^1 dS \tag{3.23}$$

This numerical source will contain the contribution to node i from all the edges surrounding the cell.

At every cell-edge k the source term is discretized in an upwind manner taking as departure point the property () used in the flux discretization

$$\delta \mathbf{U} = \sum_{m=1}^{3} \alpha_{RL}^m \tilde{\mathbf{e}}_{RL}^m \tag{3.24}$$

and

$$|\tilde{\mathbf{A}}_{RL}| \delta \mathbf{U} = \sum_{m=1}^{3} |\tilde{a}_{RL}^m| \alpha_{RL}^m \tilde{\mathbf{e}}_{RL}^m = \tilde{\mathbf{M}}_{RL} |\tilde{\mathbf{\Lambda}}_{RL}| \tilde{\mathbf{M}}_{RL}^{-1} \delta \mathbf{U} \tag{3.25}$$

Here $\tilde{\mathbf{M}}_{RL}$ is a matrix whose columns are the eigenvectors $\tilde{\mathbf{e}}_{RL}$ of the approximated jacobian $\tilde{\mathbf{A}}_{RL}$. This matrix transforms the approximated jacobian into a diagonal matrix $\tilde{\mathbf{\Lambda}}_{RL}$ with the eigenvalues $\tilde{a}_{RL}$ in the diagonal.

The source term is also decomposed into the eigenvector's basis in each edge k conforming the cell so that

$$\mathbf{H}_k^{1*} = \tilde{\mathbf{M}} \left(\mathbf{I} - |\mathbf{\Lambda}| \mathbf{\Lambda}^{-1} \right) \tilde{\mathbf{M}}^{-1} \tilde{\mathbf{H}}_k^1 = \sum_{m=1}^{3} \beta_{RL}^m \tilde{\mathbf{e}}_{RL}^m \tag{3.26}$$

represents the part of the discrete source term at edge k of cell i associated to inward normal velocity.

The average value $\tilde{\mathbf{H}}_k^1$ is computed with

$$\tilde{\mathbf{H}}_k^1 = \begin{pmatrix} 0 \\ g\tilde{h}(b_R - b_L)n_x \\ g\tilde{h}(b_R - b_L)n_y \end{pmatrix} \tag{3.27}$$

where again n_x and n_y are the components of the normal vector to edge k and $\tilde{h}$ consists of the average obtained from the depth values stored in the left and right cell that share the same edge in each computational cell

$$\tilde{h} = \frac{1}{2}\left(h_R + h_L\right) \tag{3.28}$$

Finally, the numerical scheme for this part is formulated as

$$\mathbf{U}_i^{n+1} = \mathbf{U}_i^n - \frac{\Delta t}{S_i}\left(\sum_{k=1}^{NE}\left((\mathbf{F},\mathbf{G})_k^* \cdot \mathbf{n}_k dC_k - \mathbf{H}_k^{1*}\right)\right)^n \tag{3.29}$$

3.2 Source terms: friction

Due to the small initial values (zero at initial conditions) for the variables h, u, and v and the high value of the Manning coefficient required to take into account the effects of the vegetation in the field, the friction terms become dominant and the numerical solution is affected. The main consequence is in the form of numerical stability restrictions different from the well known CFL conditions. This is further complicated by the advance of the front over dry bed. To avoid this problem, one first attempt was made to discretize the friction term in an upwind manner even though it does not show a gradient form. This option did not prove useful. Back to the pointwise option, two possibilities to avoid this problem were studied; the first is to ignore the friction terms when the depth of water is smaller than a threshold, while another approach is to treat the source terms in a semi-implicit form. The latter option is the one adopted in our case

In the approximation presented here, the friction terms are calculated in the following way

$$S_{fx} = -(1-\theta)(ghS_{fx})^{n} - \theta(ghS_{fx})^{n+1} \tag{3.30}$$

$$S_{fy} = -(1-\theta)(ghS_{fy})^{n} - \theta(ghS_{fy})^{n+1} \tag{3.31}$$

where n indicates the time level in which we know the values of the variables and $n+1$ is the next time level where we update the variables. θ is a parameter that accounts for the implicitness of the treatment of the source terms in the equation and can take any value in the interval [0,1]. We have chosen $\theta = 0.4$ for the first numerical test.

Equation (3.16) now is converted into

$$\mathbf{U}_i^{n+1} = \mathbf{U}_i^{n} - \frac{\Delta t}{S_i}\left(\sum_{k=1}^{NE}\left((\mathbf{F},\mathbf{G})_k^{*}\cdot\mathbf{n}_k dC_k - \mathbf{H}_k^{1*}\right)\right)^{n} + \Delta t\left(\mathbf{H}^{2}\right)_i^{n} \tag{3.32}$$

3.3 Source terms: infiltration

The infiltration parameters included in the source terms: i infiltration rate, D_{lx}, D_{ly} the momentum transfer due to seepage outflow are evaluated pointwise and explicitly at time level n and they do not need any special treatment.

Finally, equation (3.16) is converted into

$$\mathbf{U}_i^{n+1} = \mathbf{U}_i^n - \frac{\Delta t}{S_i}\left(\sum_{k=1}^{NE}\left((\mathbf{F},\mathbf{G})_k^* \cdot \mathbf{n}_k dC_k - \mathbf{H}_k^{1*}\right)\right)^n + \Delta t\left(\mathbf{H}^2\right)_i^n + \Delta t\left(\mathbf{H}^3\right)_i^n \tag{3.33}$$

and the complete system of equations is solved.

3.4 Advance, recession and infiltration

In order to avoid the numerical problems associated to extremely small values of water depth at the front, a procedure has been introduced so that all flow depths smaller than a certain user-defined threshold are ignored. In our case 10^{-6}m, is the minimum flow depth considered as part of the advancing front and which allows infiltration to start. If the depth is greater than the threshold, irrigation will begin at the next time step at this cell. In practical terms, every time the depth of flow is updated for a cell, the program checks whether it is smaller than this threshold. In that case it is reset to zero and this criterion is applied for both the advance and recession fronts.

Two definitions of the average velocities have been described depending on the initial conditions over which the front advances. The averages given by (3.19) are the basic ones used in wet bed case. If the flow propagates over a dry bed the modification suggested in (3.20) is enough in general.

3.5 Boundary conditions

The boundaries of the two-dimensional domain in which a numerical solution of the overland flow problem is sought are the different parts of the external contour line of the field. As in any other boundary problem in computational fluid dynamics, there is first a question concerning the number of physical boundary conditions required at every boundary point. To help, the theory of characteristics in 2D tells us that, depending on both the value of the normal velocity through the boundary

$$\mathbf{u} \cdot \mathbf{n} = un_x + vn_y \tag{3.34}$$

and the local Froude number $Fr = \mathbf{u} \cdot \mathbf{n}/c$, the possibilities are

- Supercritical inflow: $\mathbf{u} \cdot \mathbf{n} \leq -c \Rightarrow$ all the variables must be imposed.
- Subcritical inflow: $-c < \mathbf{u} \cdot \mathbf{n} \leq 0 \Rightarrow$ two variables must be imposed.
- Supercritical outflow: $\mathbf{u} \cdot \mathbf{n} > c \Rightarrow$ none of the variables must be imposed.
- Subcritical outflow: $0 < \mathbf{u} \cdot \mathbf{n} \leq c \Rightarrow$ one variable must be imposed.

A second question is related to the procedure used to obtain numerical boundary conditions.[9] In the work presented here, the idea of using a Riemann solver to calculate the flux at the face of a cell has also been used at the boundaries. The variables are stored at the centre of each cell and the boundary conditions are also imposed there. The value of the variables not prescribed are calculated from a usual finite volume balance. For this purpose, the fluxes across the edges lying on the boundary are estimated by means of a 'ghost' cell outside. Usually, the ghost cell just duplicates the boundary cell. When the boundary is a solid wall, the ghost cell is a mirror cell in which the depth of water has the same value that the boundary cell and the velocities are the same with opposite sign. Specific values of the input boundary conditions in each case are detailed in the applications section. In all the examples presented, the fields are closed almost everywhere. At the points of outflow, a free flow condition is assumed and this is modelled by means of a supercritical type boundary condition.

4 Applications

4.1 First field experiment

The experiment performed by Zapata and Playán[20] was numerically simulated. A small quadrilateral basin, 27m long by 27m wide, with an area of

729m^2 was constructed and irrigated from the southwest corner. The infiltration parameters estimated in the experiment were:

$$\begin{aligned}&k = 0.0147 m/min^a\\&a = 0.2563\\&f_0 = 0.0 m/min\end{aligned}$$

A value of 0.4 was estimated for the Manning coefficient. The field was irrigated with a constant discharge of $Q_P = 0.0093 m^3/s$ during 90 minutes. In the field experiment, observations were made of the advance and recession front.

The inflow condition has been implemented imposing the unit discharge at the center of the inflow cell in the form of the x and y components at 45^o:

$$hu = \frac{q_p}{\sqrt{2}}, \qquad hv = \frac{q_p}{\sqrt{2}} \tag{4.1}$$

where q_p is the specific discharge (m^3/sm) corresponding to QP. The water depth at the inflow point is determined by choosing the maximum value between

$$h = 1.05 \left(\frac{q_p^2}{g}\right)^{\frac{1}{3}} \tag{4.2}$$

and the water depth calculated from the mass conservation equation to avoid a supercritical inlet.

The first goal was to reproduce the advance of the water front over a flat bottom level. Figure 2 presents maps of flow depth (left) and infiltrated depth (right) at a time of 20 min. The inflow point is located at coordinates $(0, 0)$. As expected, the flow shows radial symmetry. These results

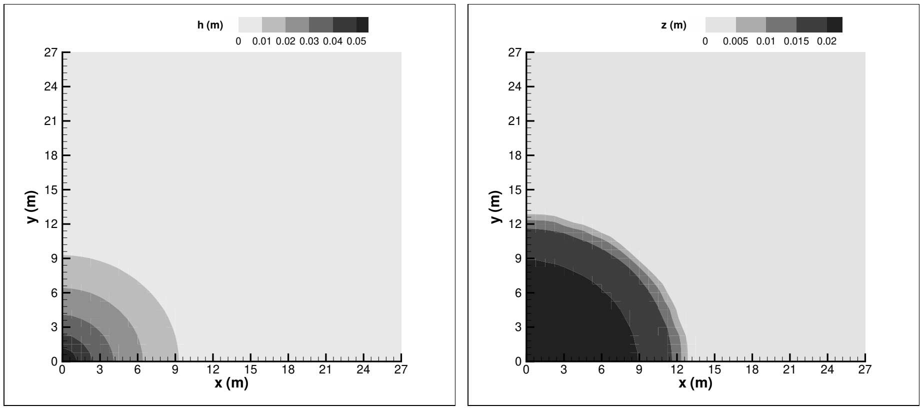

Figure 2: Maps of simulated overland (left) and infiltrated depth (right) for the first field experiment with a flat bottom configuration at time 20 min.

are coincident with the simulation output presented by Zapata and Playán.[20]

Four different calculations have been carried out using two quadrilateral meshes with $\Delta x = \Delta y = 0.75m$ (G_C), and $\Delta x = \Delta y = 0.5m$ (G_F), respectively. The bottom level is one of the variables to be stored at the center of the cells. Zapata and Playán[20] presented regular meshes reproducing the experimental bottom level (B_E) with different node spacings. Among them, those with nodal spacings of 0.75 m and 0.50 m were used in this work for G_C and G_F, respectively. Two options were possible in order to incorporate these data to the method described in the previous sections, which is essentially a cell-centered finite volume technique. One option consisted on locating the computational cell so that its vertices were coincident with elevation data. In this option, referred to as B_A, elevation data from the four vertices were averaged and stored at the cell center. The second option was to make the cell center coincident with a bottom level datum. The resulting mesh, referred to as B_L, was larger than the one obtained with the first option.

Figure 3 shows, on the left, the bottom levels in a contour line plot where dark shades of grey indicate higher zones and light shades of grey indicate lower zones. On the right, the bottom surface is represented. Both figures correspond to the G_F mesh with B_L bottom representation. All the figures showing graphically the results of this test case will be based on this mesh and bottom level representation, except when otherwise stated. At the end of this subsection two tables will summarize the numerical results obtained in all configurations.

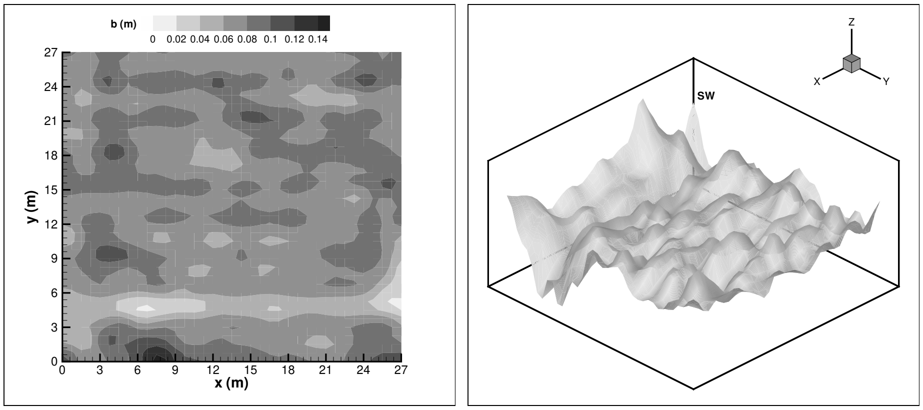

Figure 3: Contour line (left) and three dimensional (right) maps of bottom level for the first field experiment with a G_F mesh and a B_L bottom configuration.

Figure 4 presents a comparison of the observed (left) and model simulated (right) locations of the advance front at times of 20 (top) and 40 min (bottom). The simulations predict most of the features of the observed advancing front, including the channeling of the front in the depressed area running from West to East at approximately $y = 5m$. The previous simulations presented by Zapata and Playán[20] did not reproduce this channeling in such a detail and therefore provided simulations where the radial advance pattern was more evident. The model reported in this work therefore presents a significant advantage over the previous efforts to simulate this case in what refers to the location of the advancing front.

It is interesting to note how some features of the advancing front become apparent in the simulation at different times than in the field observations. This is the case of the tongue observed at 20 min for x between 15 and $21m$ and for y between 0 and $3m$. This feature is not present at the 20 min simulation, and starts to develop at time 40 min. Such disagreements should not be automatically regarded as proofs of the model inability to reproduce the real world. In our opinion, these differences are more related to the difficulty associated to measuring the bottom level accurately and to representing it in the model.

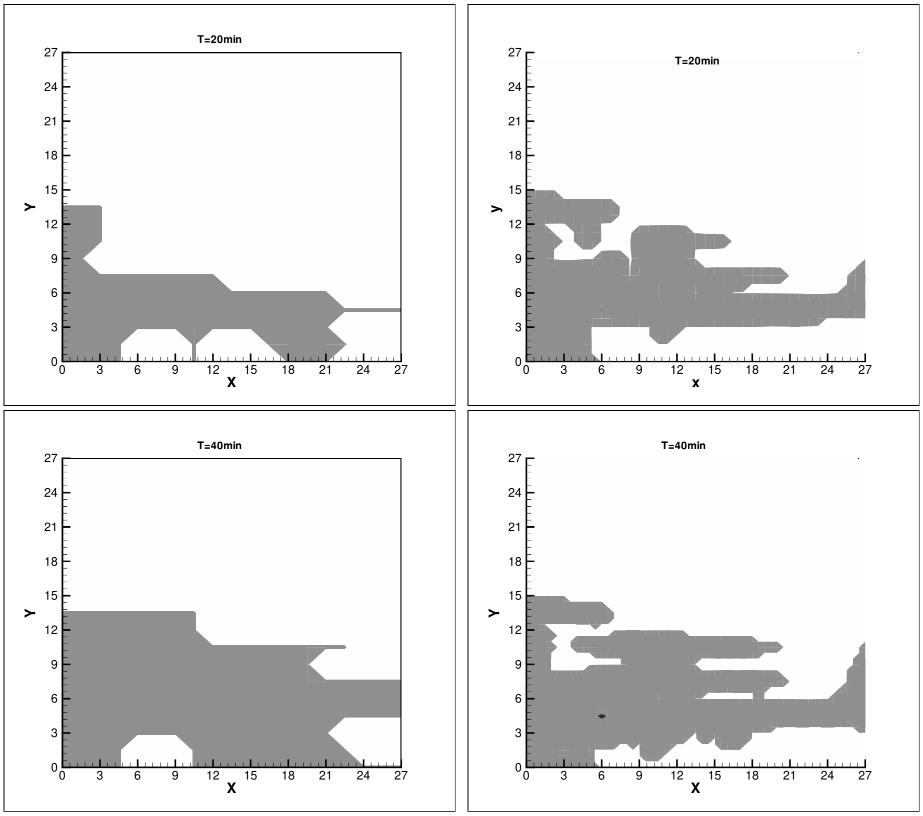

Figure 4: Location of the advancing front at times 20 (top) and 40 min (bottom) as observed (left) and simulated with the proposed model (right) for the first field experiment.

The effect of the bottom level is very relevant in this experiment. Comparisons of the observed and simulated advance with the bottom configuration (Figure 4) indicate how the flooding of the experimental field is clearly dictated by the bottom level. This is particularly true in the experimental conditions since the inflow discharge and roughness coefficient resulted low in comparison with the differences in bottom level observed in the field.

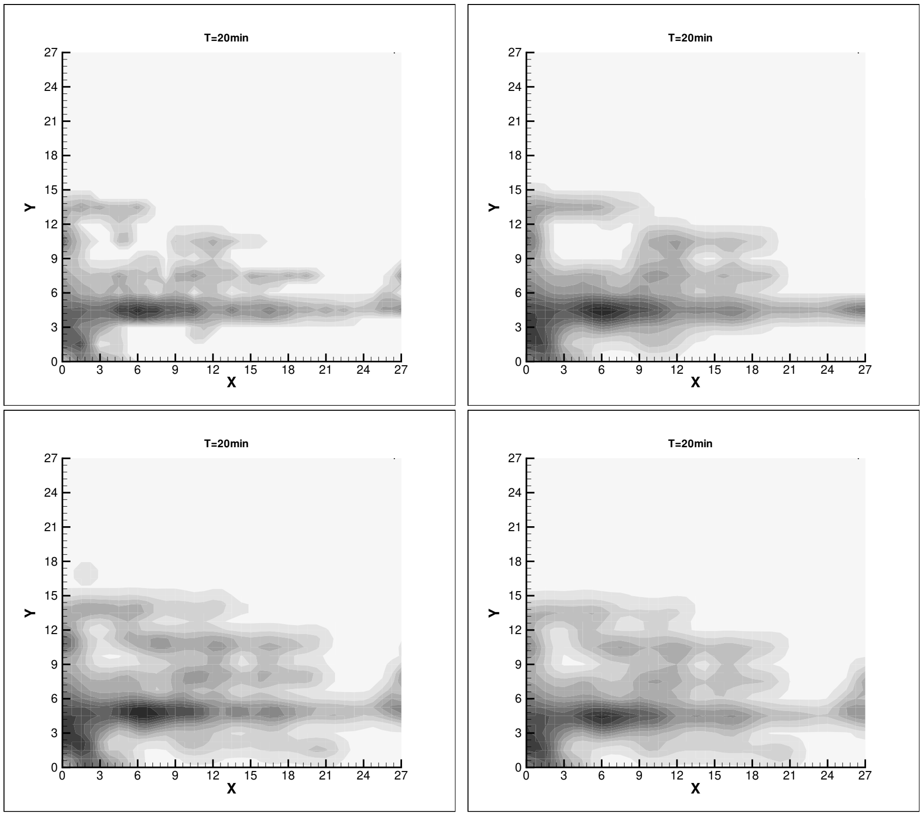

Figure 5: Contour maps of simulated overland flow depth at a time of 20 min for the first field experiment. The subfigures present the G_F (left) and G_C grids (right); and the B_A (lower) and B_L (higher) bottom level configurations.

The effect of the two grids and the two bottom configurations is presented in Figure 5, where contour maps of simulated overland flow depth are displayed for the four combinations of these two factors. The coarse grid (right) produces a significant loss of detail in the numerical simulation. At the same time, advance is faster for G_C than for G_F. The observation of this figure suggested that the fine grid resulted more appropriate for the simulation of this particular case. As for the bottom level configuration, the use of B_A results in a somewhat faster advance at the studied time. The averaging of the bottom levels produces a smoothing effect on the resulting elevation data. This can explain the faster advance.

In order to clarify the differences between grids and bottom configurations, Table 1 is provided. In this table it can be observed how the combination of G_F and B_L presents the best results for both advance and recession, and was adopted as the most accurate numerical solution.

Time	Observed	Simulated			
		G_F		G_C	
		B_L	B_A	B_L	B_A
(min)	(flooded %)	(flooded %)	(flooded %)	(flooded %)	(flooded %)
20	19	25	30	24	26
40	39	41	52	45	47
60	64	61	70	59	72
80	84	81	93	94	96
400	68	66	75	75	76
600	40	51	62	60	58
800	26	38	48	45	44

Table 1: Observed and simulated flooded percent areas at different times for the first field experiment . Simulations are presented combining the two grids (G_F and G_C) and the two bottom level configurations (B_L and B_A).

Figure 6 presents the advance (left) and recession (right) curves corresponding to the field observations and to the numerical simulations (with G_F and B_L). In both cases, the observed and simulated data show an acceptable agreement. The comparison of these results with those of previous models confirms the improvement of the predictive capability of the advance and recession processes derived from the introduction of the proposed model.

Finally, Table 2 presents the time evolution of the mass conservation error for the different combinations of grids and bottom level configurations. The figures indicate that there is little difference between the four considered cases, with slightly lower errors for the fine grid. The bottom level configuration does not have a significant effect on the simulation error. The terminal value of the mass conservation error is in the order of 1.2%.

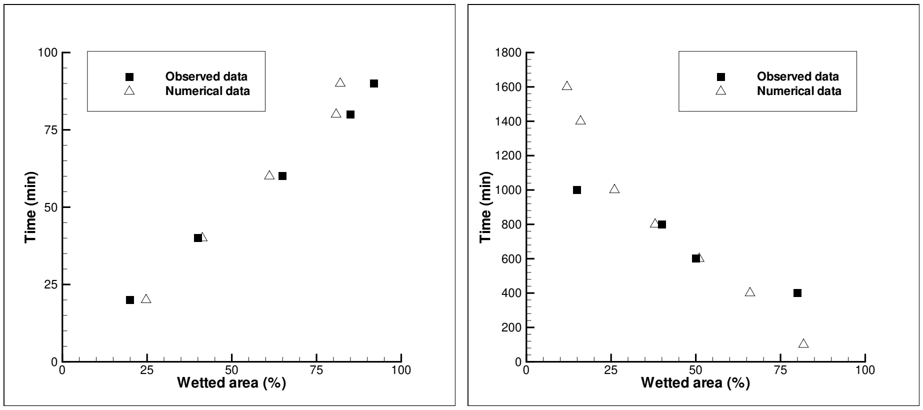

Figure 6: Advance (left) and recession (right) curves corresponding to the field observations and to the numerical simulations with G_F and B_L for the first field experiment.

Time (min)	G_F		G_C	
	B_L (error %)	B_A (error %)	B_L (error %)	B_A (error %)
20	1.4	1.4	1.7	1.6
40	1.3	1.3	1.5	1.5
60	1.3	1.3	1.5	1.5
80	1.2	1.2	1.4	1.4
400	1.2	1.2	1.4	1.3
600	1.2	1.2	1.3	1.3
800	1.2	1.2	1.3	1.3

Table 2: Time evolution of the mass conservation error for the different combinations of grids and bottom level configurations in the first field experiment.

4.2 Second field experiment

A second experiment was performed for the purpose of testing the proposed model. For this purpose, additional data were collected on the irrigation event of basin number 2 cited in Zapata et al.[21] A detailed bottom level survey was performed, and a non-structured grid was used with 440 triangular cells. Due to the irregular field shape, a triangular numerical grid was chosen. The bottom level of the individual cells was obtained averaging the experimental data recorded at the triangle vertices and stored at the center.

The basin was almost rectangular with an area of $5,792m^2$. The infiltration parameters estimated in the experiment were:

$$k = 0.0030m/min^a$$
$$a = 0.5336$$
$$f_0 = 0.0m/min$$

A value of 0.2 was estimated for the Manning coefficient. Irrigation water entered the basin through two inflow points located at the Northwest (NW) and Northeast (NE) basin corners. Both inflows started at the onset of the irrigation event. Discharge at the NW was almost constant at $0.093m^3/s$, lasting for $85min$. The inflow hydrograph through the NE corner was bell-shaped, with a peak discharge of $0.027m^3/s$ at a time of $41min$, and lasting for $137min$. The inflow condition was implemented imposing the unit discharge variables at the center of the inflow cell situated at the northwest and northeast corners of the irrigated field and the depth was calculated as described in the above subsection. In the field experiment, observations were made of the time of advance at selected points.

Figure 7 shows the bottom level of the analyzed basin presented as a contour line map (left) and as a three-dimensional map (right). Figure 8 presents maps of overland flow depth (left) and bottom level plus overland flow depth (right). Maps are provided for times of 15 (top), 45 (middle) and $90min$ (bottom). The figures present the advancing fronts derived from the two inflow points. The configuration of the advancing fronts is dictated by the bottom level. This is particularly true for the advance from the NE inflow, whose discharge is lower.

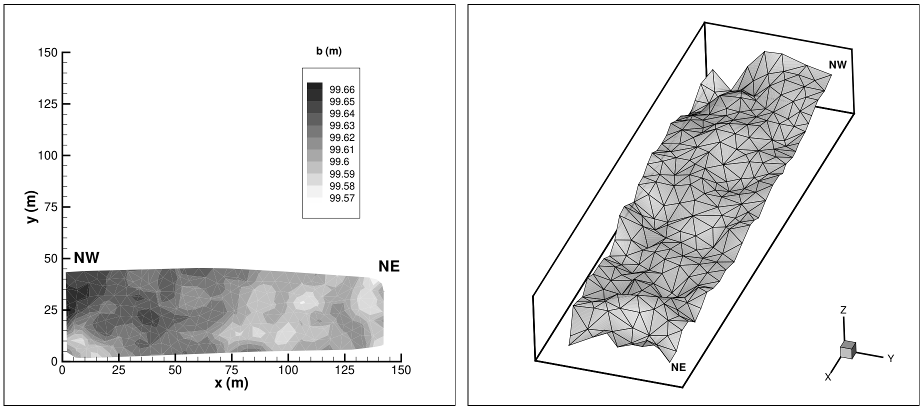

Figure 7: Contour line (left) and three dimensional (right) maps of bottom level for the second field experiment.

The areas covered by water at the NW and NE areas at times 15 and $45min$ reflect the differences in discharge among both inflows. At time $90min$ the discharge from the NE inflow is very low, and the area covered by water is actually smaller than it was at time $45min$. In fact, the area covered at $45min$ appears now divided in two, with the appearance of a recession line at $x = 125m$, due to a local high spot. At this time the flooded area west of this recession line has collided with the advancing front derived from the NW inflow. This second field experiment shows the capability of the numerical model to deal with the successive flooding and unflooding of the computational cells. A comparison (for a given time) of the left and right subfigures reveals how the somehow erratic behavior of the flow depth becomes smooth when the bottom level is added and the free water surface level is mapped (right subfig.), providing satisfactory simulations to the field experiment.

In the last figure (Fig. 9) the observed and simulated time of advance to some points located along the experimental fields are compared. A 1:1 slope line is included in the plot for comparison purposes. The data set for this figure includes points flooded by both inflow points. The scatter plot surrounds the diagonal line, indicating that advance was not systematically over- or underestimated by the proposed model.

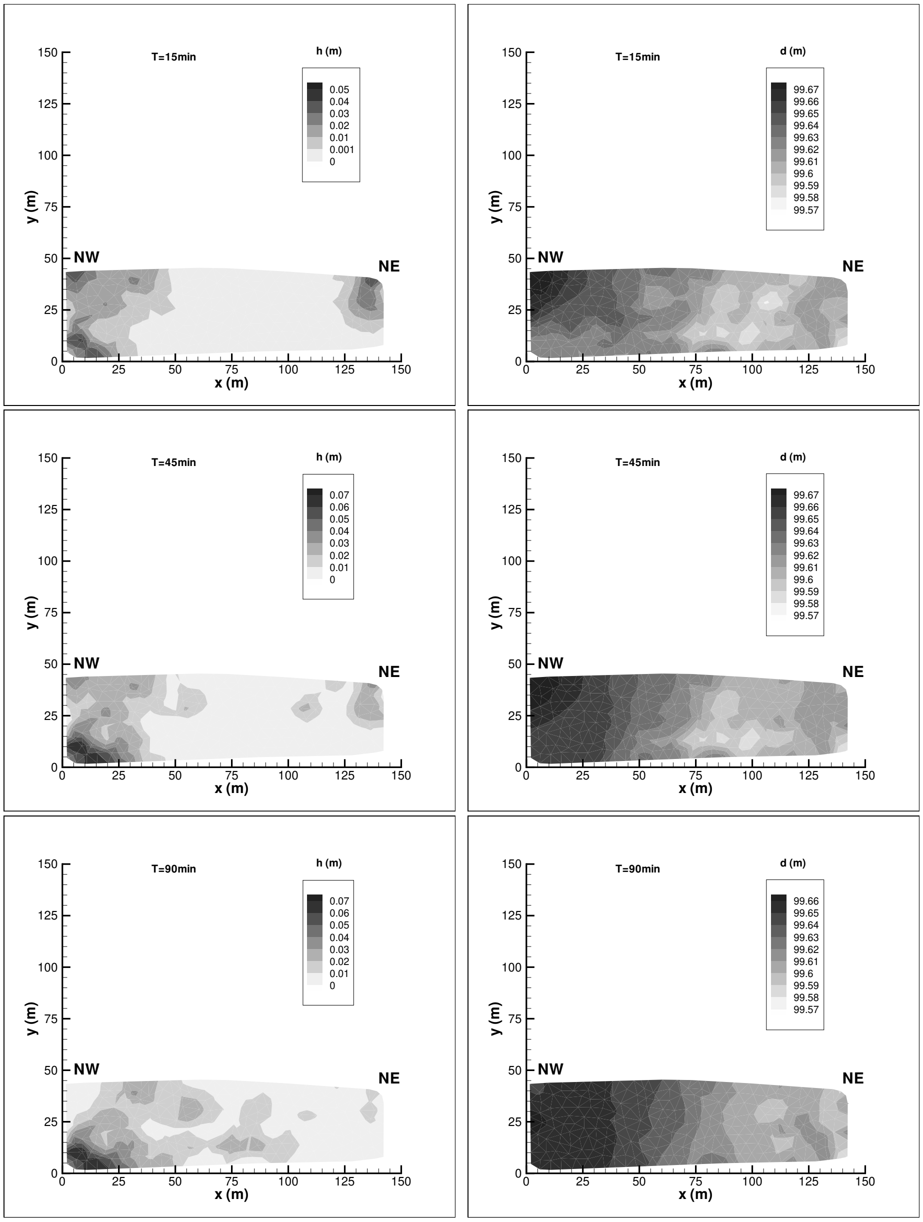

Figure 8: Contour line maps of overland flow depth (left) and bottom level plus overland flow depth (right) at simulation times of 15 (top), 45 (middle) and 90min (bottom) for the second field experiment.

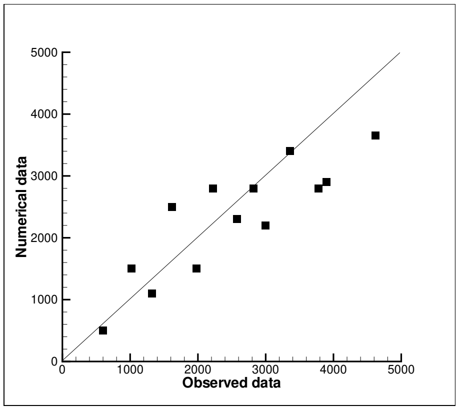

Figure 9: Simulated vs. observed time of advance to some points in the second field experiment. Solid line represents 1:1

5 Conclusions

A finite volume based upwind scheme has been presented and applied to the numerical simulation of overland flows for irrigation purposes. The procedure is independent of the structured or unstructured character of the mesh. The flow problem is characterized by a thin water layer and the movement is governed by the advection terms as well as by the source terms in the equations. The numerical treatment of both has been emphasized in the work presented. Strong bottom variations and high values of the roughness coefficient made necessary the application of more careful treatment of the corresponding terms in the equations to avoid numerical instabilities in the solution.

Two cases of interest in Agricultural Engineering have been chosen to evaluate the performance of the numerical technique, both based on field experiments. The simulation of the first field experiment has improved previous results, providing a more realistic representation of the hydrodynamics of basin irrigation, particularly in what refers to the location of the advancing front. This experiment has been applied to the identification of the grid fineness requirements and to the determination of proper handling procedures for the bottom level. In this particular case, a fine, non-averaged grid proved to yield the best results. The second field experiment has been used to illustrate the application of the model to the use of inflow hydrographs and to the simulation of colliding fronts.

Acknowledgements

The authors would like to thank the CONSID-DGA for providing the funding for this research under research project P-08/96.

List of Tables

List of Figures

Bibliography

[1] M.B.Abbott, *Computational Hydraulics*, Ashgate Pub. Comp., 1992.

[2] A.A.Akanbi and N.D.Katopodes, "Model for flood propagation on initially dry land", *J. Hydr. Div.*, ASCE, **114(HY7)**:689–706, 1988.

[3] A.Bermúdez and M.E.Vázquez, "Upwind methods for hyperbolic conservation laws with source terms", *Computers Fluids*, **23(8)**:1049–1071, 1994.

[4] A.Bermúdez, A.Dervieux, J-A.Desideri and M.E.Vázquez, "Upwind schemes for the two-dimensional shallow water equations with variable depth using unstructured meshes", *Comput. Methods Appl. Mech. Engrg.*, **155**:49–72, 1998.

[5] V.T.Chow, *Open channel hydraulics*, MacGraw-Hill Book Co. Inc.,1959.

[6] A.J.Clemmens and T.Strelkoff, "Dimensionless advance for level-basin irrigation", *J. Irrig. Drain. Div.*, ASCE, **105(IR3)**:259–273, 1979.

[7] J.A.Cunge, F.M.Holly and A.Verwey, *Practical aspects of computational river hydraulics*, Pitman, 1980.

[8] P.Glaister, "Prediction of supercritical flow in open channels", *Comput. Math. Applic.*, **24(7)**:69–75, 1992.

[9] Ch.Hirsch, *Numerical computation of internal and external flows*, John Wiley and Sons, New York, 1990.

[10] R.J.LeVeque, "Balancing source terms and flux gradients in high-resolution Godunov methods: the quasi-steady wave-propagation algorithm", *J. Comput. Phys.*, **146(1)**:346–365, 1998.

[11] E.Playán, W.R.Walker and G.P.Merkley, "Two-dimensional simulation of basin irrigation. I: Theory", *J. Irrig. Drain. Div.*, ASCE, **120(5)**:837–856, 1994.

[12] E.Playán, J.M.Faci and A.Serreta, "Modeling microtopography in basin irrigation", *J. Irrig. Drain. Engrg*, ASCE, **122(6)**:339–347, 1996.

[13] A.Priestley, "Roe-type schemes for super-critical flows in rivers", Numerical Analysis Report 13/89, Department of Mathematics, University of Reading, 1989.

[14] P.L.Roe, "Approximate Riemann solvers, parameter vectors, and difference schemes", *J. Comput. Phys.*, **43(2)**:357–372, 1981.

[15] P.L.Roe, "A Basis for Upwind Differencing of the Two-Dimensional Unsteady Euler Equations", *Num. Met. Fluid Dyn. II*, Oxford Univ. Press (1986).

[16] P.K.Smolarkiewicz and L.G.Margolin, "MPDATA: a finite-difference solver for geophysical flows", *J. Comput. Phys.*, **140**:459–480, 1998.

[17] V.Singh and S.M.Bhallamudi, "Hydrodynamic modeling of basin irrigation", *J. Irrig. Drain. Div.*, ASCE, **123(6)**:407–414, 1997.

[18] B.Van Leer, "Towards the ultimate conservative difference scheme V. A second order sequel to Godunov's method", *J. Comput. Phys.*, **32**:101–136, 1979.

[19] W.R.Walker and G.V.Skogerboe, *Surface irrigation. Theory and practice*, Prentice-Hall, Inc., Englewood Cliffs, New Jersey. 386 pp 1987.

[20] N.Zapata and E.Playán, "Simulating elevation and infiltration in level-basin irrigation" *J. Irrig. Drain. Engrg.*, ASCE, **126(2)**:78–84, 2000.

[21] N.Zapata, E.Playán and J.M.Faci, "Water reuse in sequential basin irrigation", *J. Irrig. Drain. Engrg.*, ASCE, in press, 2000.